

# Microstructural Evolution in the Heat-Affected Zone of a Friction Stir Weld

R.W.Fonda<sup>1</sup> and J.F. Bingert<sup>2</sup>

<sup>1</sup>*Naval Research Laboratory, Washington, DC*

<sup>2</sup>*Los Alamos National Laboratory, Los Alamos, NM\**

*\*on change-of-station to Naval Research Laboratory*

## Abstract

The microstructure and crystallographic texture spanning the soft region at the TMAZ/HAZ boundary of a friction stir weld in 2519 Al were systematically investigated to determine their contributions to the properties of that region. The microstructure was shown to be the primary cause of softening at the TMAZ/HAZ boundary. During welding, fine  $\theta'$  precipitates responsible for much of the strength in this alloy coarsen and transform to the equilibrium  $\theta$  phase in the HAZ and into the TMAZ, accounting for the observed softening through the HAZ region. The higher temperatures achieved in the TMAZ partially re-solutionize the precipitates and allow the subsequent formation of GP zones during cooling. These two processes are responsible for the variation in microhardness observed in the TMAZ/HAZ region. Texture analyses revealed significant differences in the crystallographic texture across this region that were primarily due to macroscopic rigid-body rotations of the grains, but do not account for the observed softening. The effect of the observed microstructural evolutions on the friction stir welding deformation field and on the fracture behavior of the weld are also discussed.

## **I. Introduction**

Friction stir welding (FSW) is a solid-state joining technique developed at TWI in 1991<sup>[1]</sup>. With this technique, a rotating, non-consumable tool consisting of a small-diameter pin extending down from a larger diameter shoulder is plunged into the joint line and is then traversed along that line. Insertion of the rotating pin heats the surrounding material, allowing it to be deformed by the motion of the pin and causing some extrusion above the surface. Further insertion brings the shoulder into contact with the workpiece, constraining the extruded material and providing additional frictional heating around the inserted pin. This rotating tool is traversed along the joint line, continuously heating the material around the tool and deforming ("stirring") that softened material together. Although temperatures approaching the melting temperature will be achieved during friction stir welding, FSW is a solid-state process; no melting occurs during this processwelding.

The heat and deformation generated during FSW produce microstructurally distinct regions across the weld. The outermost portions of the weld were modified by the thermal field of the welding process yet did not experience any deformation. This region is called the heat affected zone (HAZ) and is similar to heat-affected zones observed in welds prepared by more conventional fusion welding processes. Inward from the HAZ is located the thermo-mechanically affected zone (TMAZ), where the material experienced plastic deformation due to the stirring process in addition to the heat-induced microstructural changes. At the center of the weld, where the heat and deformation were the greatest, aluminum alloys undergo dynamic recrystallization within an onion-shaped region called the weld nugget, which is approximately the size of the rotating pin of the tool.

In whole-weld tensile tests, most precipitation-strengthened aluminum alloys exhibit similar yielding and fracture behavior<sup>[2-5]</sup>. During these tests, the tensile strain becomes localized in the HAZ on both sides of the weld nugget<sup>[6]</sup>. Fracture will typically occur at this location and will usually be located on the retreating side of the weld (the side where the tool rotation is opposite to the pin translation or welding direction)<sup>[5]</sup>.

The localization of yield and fracture at the HAZ demonstrates the importance of this region in controlling the mechanical behavior of friction stir welds. Despite this, there have been few systematic examinations of the HAZ to determine the underlying cause of this behavior. Some studies<sup>[2-4,7-10]</sup> have demonstrated that precipitates are significantly coarsened in the HAZ relative to those observed in the unaffected base plate and/or weld nugget. Sato, *et al.*<sup>[11]</sup> examined different locations in the HAZ and weld nugget of a 6063 Al FSW, and observed that the precipitates experienced increasing dissolution towards the weld center. Su, *et al.*<sup>[12]</sup> recently reported on precipitate evolutions occurring in a 7050 Al FSW. They observed a coarsening of precipitates from the base plate into the TMAZ, with increasing dissolution and reprecipitation occurring from the TMAZ into the weld nugget. In the current study, the microstructural evolution and crystallographic texture are systematically characterized as a function of position across the HAZ/TMAZ boundary of a 2519 Al FSW.

## **II. Experimental**

The friction stir weld was prepared by the Navy Joining Center of Columbus, Ohio. Two plates of 25 mm (1 inch) thick 2519-T87 aluminum were friction stir welded along the rolling direction with a conventional pin tool under load control. The welding was performed with a

rotational speed of 175 rpm and a tool translational speed of 1.1 mm/s (3.5 inches/min). This weld was sectioned normal to the weld direction (WD), and the transverse cross section was polished and then etched with Keller's reagent to reveal the microstructure. Transverse tensile properties were measured at three locations along the weld by the Navy Joining Center according to ASTM E8. The tensile bars, which spanned the weld and HAZ regions with a 12 mm x 12 mm (1" x 1") cross section, all exhibited similar tensile properties and fracture behavior.<sup>[13]</sup>

Microhardness measurements were acquired across this transverse cross section, after re-polishing the surface, with a 200 g load and a 0.5 mm spacing using a LECO Automated Microindentation Hardness Testing system. Additional microhardness measurements demonstrated that there was no interaction between adjacent indents even at one-half this spacing. Color microhardness maps were constructed from the microhardness data and then superimposed on the weld cross-section to enable a direct correlation between the microstructural regions of the FSW and the microhardness of those regions. Etching the indented surface resulted in an improved correlation between the microstructure and the microhardness map.

Four regions spanning the soft band at the HAZ/TMAZ boundary (HAZ, HAZ/TMAZ boundary, outer TMAZ, and middle of TMAZ) were selected for detailed examination and comparison to the unaffected base plate by transmission electron microscopy (TEM) and electron back-scattered diffraction (EBSD) analysis. All analyses were performed on the same plane of observation (the transverse cross section) as for the optical microscopy samples. Cylindrical samples from these four regions and the base plate were cored out along the weld direction using a 3 mm ID cylindrical electrode on a U.S. EDM Model D55 electro-discharge machine. Slices from these samples were mechanically thinned to 100  $\mu\text{m}$  and then electropolished in a

Fischione twin-jet electropolisher for examination in a Philips CM-30 TEM operating at 300 kV. Electropolishing was performed with a solution of 30% nitric acid in methanol at  $-30^{\circ}\text{C}$  with a current of about 67 mA, corresponding to approximately 23 V. TEM imaging of these five regions was performed at the same magnification using similar imaging conditions ( $g = 022$  near a  $[100]$  zone axis) to facilitate comparisons between the microstructures of these regions.

Samples for EBSD analyses were prepared in a similar fashion, except they were electropolished for a shorter time to minimize curvature of the surface and prevent perforation at the center. EBSD data were collected on LEO 1550 and Philips XL30 field-emission scanning electron microscopes equipped with a DigiView 1612 CCD camera and using TSL software<sup>[14]</sup>. At least two scans were performed for each region: a lower resolution ( $8\text{ }\mu\text{m}$  step size) scan of the central  $1\text{ mm} \times 1\text{ mm}$  portion of each sample to measure the average texture of those regions and a higher resolution ( $0.35$  to  $0.85\text{ }\mu\text{m}$  step size) scan to delineate the substructure. Texture analyses were performed with TSL software and the popLA texture package<sup>[15]</sup>.

### **III. Results & Discussion**

The friction stir weld examined in this study, shown in Figure 1a, exhibits a morphology typical of most friction stir welds. At the center of the weld, the nugget displays characteristic concentric rings in its interior and a well-defined outer edge on the advancing (left) side. The dark region on either side of the weld nugget corresponds to the TMAZ. At higher magnifications, the grains in this region can be seen to deflect upward towards the weld center from their horizontal orientation in the HAZ and base plate material. The HAZ is located outside of the TMAZ, but cannot be distinguished from the base plate under these imaging conditions.

### *i) Microhardness*

In order to examine the property variations across the weld, the microhardness was measured across the two-dimensional transverse cross section at a spacing (vertical and horizontal) of 0.5 mm and then plotted on a microhardness map as shown in Figure 1b. This microhardness map demonstrates that both the weld nugget and the flow arm (the region across the top of the weld) have a microhardness just below that of the base plate. The most conspicuous feature of this microhardness map is the two soft bands that extend diagonally from the base of the weld nugget. These soft bands appear to correlate to the “corrosion zone” observed in some other aluminum alloys<sup>[6]</sup>. Figure 1c shows the result of superimposing the microhardness data onto the structural data from optical imaging (Fig. 1a). This view permits correlation between microstructural and microhardness detail in the weld.

The data from this microhardness map can be used to evaluate the asymmetry of the weld. Subtracting the microhardness of the retreating side of the weld from that of comparable positions on the advancing side yields a map of the microhardness difference as a function of position in the weld, as shown in Figure 2. This difference map demonstrates that there is little variation between the advancing and retreating sides of this weld except at the outer edge of the weld nugget. The asymmetry is most pronounced near the mid-plane of the weld and extends across a greater area towards the base of the weld. This characteristic asymmetry is also evident in Figure 1b, which shows that the microhardness of the advancing side of the weld nugget is retained out to the edge of the weld nugget, whereas the microhardness of the retreating side decreases from the weld center to the edge of the weld nugget. The sharpness of the weld nugget boundary in images of the weld cross section (Figure 1a) also displays this asymmetry. The

advancing side of the weld nugget is typically sharp and readily discernable whereas the retreating side of the weld nugget is much more diffuse.

The variations in microhardness can be directly correlated to locations in the weld by overlaying the microhardness map on the image of the weld cross section. The superposed image, shown in Figure 1c, reveals the location of the soft band to be at the boundary between the HAZ and the TMAZ, where the horizontal, pancaked grains of the HAZ deflect upward into the stirred region of the TMAZ. This HAZ/TMAZ boundary also corresponds to the fracture location in whole weld transverse tensile tests (see Figure 3). The majority of grains inside (closer to the weld center) the fracture line are inclined, while most grains outside that line remain undeformed. The correlations among the high grain curvature, the low microhardness, and the fracture localization all occurring at the HAZ/TMAZ boundary suggest that grain/subgrain structure, crystallographic texture, and precipitate overaging could all contribute to the observed softening at this location. The objective of this research was to systematically examine the variation of these factors across the soft band in order to determine the primary causes of that soft band and the fracture associated with it.

In order to examine the variations across the soft band in a systematic manner, detailed microstructural examinations were conducted on specific locations spanning the soft band. The locations of these specimens, both on the transverse cross section and relative to hardness linescans through their location, are shown in Figure 4. These locations correspond to the heat affected zone (HAZ), the center of the soft band (SB), which corresponds to the point of greatest deflection of the grains, the outer portion of the thermo-mechanically affected zone (oTMZ), and the middle of the TMAZ (mTMZ). An additional location was examined in the unaffected base plate (BP) for comparative purposes.

## *ii) Grain structure and Crystallographic Texture*

The crystallographic textures of the various regions were investigated by automated electron backscattered diffraction (EBSD) mapping. This technique<sup>[16]</sup> measures the spatially resolved texture of specific regions, and can also be used to image the substructure within those regions by delineating misorientation boundaries within the microstructure. For each FSW region under consideration, a coarse-scale scan was performed over a 1 mm<sup>2</sup> area in order to determine a representative local texture. Figure 5 shows a series of 111 pole figures calculated from the EBSD data for the locations on the retreating side of the weld indicated in the transverse cross-section image. The elongated morphology of grains in the BP provides a means to estimate the macroscopic rigid-body rotation encountered during FSW due to the gross stir-induced flow of material surrounding the nugget. Blocks of grains are tilted in concert such that the sample reference frame, in this case defined by the grain axes, is rotated with respect to the external reference frame. This apparent grain inclination was determined for each region (and is indicated on the transverse cross section shown in Figure 5) based on a visual estimation of the angular deviation of the major axis of grains from the horizontal plane. The EBSD-derived microstructures for the five regions were then rotated about the axis defined by the WD in order to visually match the EBSD-derived microstructures to the optical results. The textures of these regions, represented by the 111 pole figures in Fig. 5, appeared qualitatively similar although rotated. This permitted a rough estimate of rotation based on the texture of each region, and these are listed with their associated pole figures. The magnitude of the pole figure rotations correlates moderately well (average deviation is 6.5°) with those measured by the grain inclination. Since the pole figure rotations roughly follow the morphologic rotations of the



grains, this qualitatively suggests that the dominant source of orientation change from the BP through the TMAZ is due to a rigid-body rotation of grains about the WD.

In order to more quantitatively assess the texture and test the assumption of rigid-body rotation dominance of texture evolution, the orientation distribution function (ODF) was calculated for each region. A rotation corresponding to the measured grain inclination was first applied to the orientation data to compensate for the rigid-body rotation. This was done to segregate the macroscopic rigid rotation effects associated with the bulk movement of material surrounding the stir zone from any texture evolution resulting from plastic deformation. Any remaining change in the ODF would then be due to internal slip and resultant plastic spin (along with the possibility of local rigid rotations that are coupled to simple shear deformation gradients). For this analysis we assumed that the macroscopic rigid-body rotation was limited to rotations about the WD. This assumption both reflects the observed grain rotations and is consistent with the observed texture. Orthotropic sample symmetry was applied to the texture data after the rotations. The  $\varphi_2 = 0^\circ$  and  $45^\circ$  sections (Bunge notation) of the ODF from each region are shown in Figure 6. Locations of some low-index orientation fibers are identified in the BP sections. As the material is extruded upward into the stir zone, some plastic deformation is anticipated, and indeed is suggested by moderate changes in the ODF. The mTMZ region exhibits the greatest deviation in rotation-adjusted texture from the BP; this is due to increased plastic deformation and/or additional rotation components present farther into the stir zone. However, the difference among rotation-adjusted textures is less than that produced by the rotation itself. An additional ODF calculation on the rotated regions with respect to the ND showed that the (001) and (110) planes remain roughly aligned with the original broad surface of the grains, while evolution in the mTMZ region shows a trend toward development of (111)

parallel to the grain face. The latter effect may be the result of simple shear deformation on the steeply inclined mTMZ grains.  $\langle 100 \rangle$  is the dominant direction parallel to WD, although this also begins to migrate toward  $\langle 110 \rangle$  in the mTMZ. Overall, these results suggest that macroscopic rigid-body rotation provides the dominant effect on texture evolution through the TMAZ, but plastic spin provides increasingly greater contributions as the TMAZ/nugget boundary is approached.

Higher-resolution EBSD scans were also performed within the same regions to investigate the substructure development. Results are shown in the form of image-quality maps in Figure 7. The image quality is determined by the intensity of the detected peaks from the transformation of the diffraction pattern. All other parameters (grain orientation, chemistry, *etc.*) being equal, lower IQ regions (darker shading in the maps) denote areas of greater crystalline distortion and therefore greater dislocation density. Boundary regions will also display lower IQ values due to the partitioning of the diffraction pattern between neighboring orientations. High-angle boundaries (HABs), identified here as misorientations greater than  $15^\circ$ , are delineated by heavy black lines in the IQ maps, while low-angle boundaries (LABs) with between  $2^\circ$  and  $15^\circ$  misorientations are shown as light lines. For the HAZ in Fig. 7a, coarse precipitates are present within a hot-rolled microstructure that is otherwise equivalent to that observed for the BP. Figure 7b shows an IQ map of the SB region intermediate between the HAZ and oTMZ. Evidence of incipient deformation can be observed in the form of LABs, primarily concentrated at pre-existing grain boundaries. This heterogeneous distribution of deformation-induced structure suggests plasticity is preferably accommodated at boundary regions. The increased deformation activity observed in the oTMZ and mTMZ IQ maps is consistent with the progressive deviation of TMAZ textures away from the BP condition shown in Fig. 6. Boundary

serrations, a microstructural feature generally associated with dynamic recovery processes, are also evident in the mTMZ structure.

In order to determine the potential effect of the texture evolution on mechanical strength, the volume-averaged Taylor factor for each region was computed. The Taylor factor ( $M$ ) for uniaxial deformation can be expressed as:

$$M = \frac{\sigma}{\tau_c} = \frac{\sum \tau_i}{\sigma} \quad (1)$$

where  $\sigma$  is the flow stress under uniaxial loading,  $\tau_c$  is the critical resolved shear stress for the active slip system,  $\sum \tau_i$  is the total internal shear strain summed over each of the active slip systems, and  $\epsilon$  is the external uniaxial strain. Under Taylor's original model<sup>[17]</sup>, the set of active, independent slip systems is identified for an increment of external strain so as to minimize internal shear while maintaining strain compatibility between grains in a polycrystal. Therefore, Eq. 1 effectively provides a measure of the orientation dependence of plastic deformation. Larger values of  $M$  denote orientations more resistant to plastic deformation under a specified strain path. An average  $M$  ( $\bar{M}$ ) was determined for each region assuming uniaxial deformation in the transverse direction (TD), analogous to the tensile test configuration resulting in failure along the SB (see Fig. 3). A comparison of  $\bar{M}$  to the microhardness variation requires the calculation of  $M$  under compressive loads normal to the section plane (along WD). In both cases,  $\{111\}\langle 110 \rangle$  slip systems of equal  $\tau_c$  were assumed to be operative. Taylor factors were calculated within both the TSL analysis package and with the orientation data input to the Los Alamos polycrystal plasticity (LApp)<sup>[18]</sup> code; results were substantially similar. Results are shown in Figure 8 as a notated cross-section of the weld. The distribution of  $\bar{M}$  for deformation in the TD and WD is narrow, with values near that for a random fcc polycrystal (3.07), which is

not surprising considering the fairly weak and self-similar textures. For the WD-compression deformation, these results show a slight decrease in  $\overline{M}_{WD}$  in the SB and oTMZ, although of a magnitude that suggests only a second-order effect on the large variation in microhardness. For tensile deformation in the TD, the  $\overline{M}_{TD}$  of the SB region is intermediate between those observed in the mTMZ and the nugget. It would therefore appear that the mechanical property degradation of the SB region, and its associated weak-link behavior under transverse tension, are not a function of texture.

### *iii) Precipitate Distributions*

The friction stir welding process introduces significant heat into the region surrounding the weld. Figures 9 through 14 illustrate the effect of this heat input on precipitate distributions near the soft band. Far from the weld, the unaffected baseplate (Figure 9a) exhibits a dense distribution of fine  $\square'$  precipitates, which are responsible for the good mechanical properties of this alloy. These precipitates lie on  $\{100\}$  planes of the matrix and have a plate morphology with an average diameter of approximately 50 nm. In this imaging condition, two orientation variants are apparent at  $90^\circ$  to each other while the third orientation variant, which is in plan view, cannot be clearly resolved. The reflections from these precipitates in electron diffraction patterns (Figure 9b) are elongated, indicating that the  $\square'$  precipitates are very thin. The locations of typical precipitate diffraction reflections and double diffraction effects for this alloy are given in Figure 10.

In the HAZ (Figure 11), the  $\square'$  precipitates experience a dramatic decrease in concentration accompanied by a significant increase in size. The precipitates in the HAZ are approximately 100 nm in diameter, about twice the size that was observed in the base plate. Both the apparent

thickness of precipitate plates in the images (Figure 11b) and the sharpness of the  $\beta'$  precipitate reflections in the electron diffraction patterns (Figure 11c) demonstrate that these precipitate plates have experienced significant thickening during coarsening when compared to the base plate (Figure 9). Coarser precipitates with an irregular shape and orientation are also present in this region of the HAZ. These additional precipitates are identified by electron diffraction as precipitates of the equilibrium  $\beta$  phase.

The microstructure in the soft band (Figure 12) displays a similar trend. The higher temperatures achieved in this region have caused an increase in the  $\beta$  precipitation, relative to that seen in the HAZ. Since there is a precipitate free zone around each  $\beta$  precipitate, this corresponds to an overall decrease in the number of  $\beta'$  precipitates. This is reflected in electron diffraction (Figure 12c), which shows a stronger intensity of the  $\beta$  precipitate reflections relative to the  $\beta'$  precipitate reflections. While the remaining  $\beta'$  precipitates only have a slightly larger diameter than in the HAZ, they experienced a significant thickening. The thickness of  $\beta'$  precipitates in the soft band is approximately 20 nm (Figure 12b), almost double that observed in the HAZ (Figure 11b).

It needs to be noted that the images shown in Figures 9 through 14 are of typical microstructures with a similar sample thickness. Because the sample thickness was not measured, quantitative comparisons between these images are not possible. However, the microstructural variations between these regions are significant and are reflected in the electron diffraction patterns, which accurately reflect the volume fractions of the constituent precipitate phases relative to the matrix and each other. Thus, the images are provided as a qualitative illustration of the microstructural variations between the regions, while the electron diffraction patterns provide a quantitative basis for those comparisons.

The precipitate distributions in the outer portions of the TMZ (Figure 13) differ significantly from those present in the HAZ or SB. The most apparent difference is in the much lower density of  $\beta'$  precipitates in the oTMZ. The actual density varies from regions almost devoid of  $\beta'$  precipitates to the  $\beta'$  precipitate density shown in Figure 13a. The higher temperatures experienced in this region have caused the  $\beta'$  precipitates to coarsen further than in regions further from the weld. Although the thickness of the  $\beta'$  precipitates is comparable to what was observed in the SB, these  $\beta'$  precipitates have an average diameter of over 150 nm, about a third larger than the precipitates in the SB. These precipitates also have a narrow size distribution, with few precipitates having a diameter of less than 150 nm. The coarsening of the  $\beta'$  precipitates is accompanied by an increase in both the number density and size of precipitates of the equilibrium  $\beta$  phase. These trends are illustrated in the electron diffraction pattern (Figure 13c). Electron diffraction patterns from this region display an increased intensity of the  $\beta$  reflections coupled with a decreased intensity of the  $\beta'$  reflections, which are not visible in this image.

In the middle of the TMZ (Figure 14), only the equilibrium  $\beta$  precipitates were observed; no  $\beta'$  precipitates were observed in this region. The  $\beta$  precipitates in this region exhibit a more uniform, but smaller, size distribution and a higher number density than in the outer portion of the TMZ (compare Figures 14a and 13a), indicating that the higher temperatures experienced by this region resulted in an increased nucleation rate as well as increased dissolution of the  $\beta$  precipitates. The electron diffraction patterns from this region (Figure 14c) exhibit strong reflections from the  $\beta$  precipitates but no intensity from the  $\beta'$  precipitates, reflecting these observations.

While the coarsening and transformation of the  $\theta'$  precipitates seen in Figures 9 to 14 would seem to indicate a consistent softening of the alloy from the base plate to the TMZ, the microhardness data (Figure 4) shows a gradual increase in the microhardness from the HAZ/TMZ boundary towards the center of the weld. The cause of this apparent discrepancy is revealed in the diffuse streaking between the matrix reflections in Figures 13 and 14. This streaking is evidence of the formation of very fine precipitates, called Guinier-Preston or GP zones<sup>[19,20]</sup>, on  $\{001\}$  matrix planes. Direct imaging of these GP zones demonstrates that they have a size of less than 10 nm in the middle of the TMAZ. Precipitation of these GP zones increases with distance inside the HAZ/TMAZ boundary, as evidenced by the more intense streaking between matrix reflections in the electron diffraction patterns seen in the middle and outer regions of the TMAZ. This increased precipitation produces the observed increase in microhardness from the HAZ/TMAZ boundary towards the center of the weld.

The microstructural trends displayed in Figures 9 through 14 typify the aging sequence generally observed in Al-Cu alloys<sup>[21]</sup>. Lower temperatures cause the fine  $\theta'$  precipitates to coarsen and to transform to  $\theta$ , lowering the microhardness of those regions. Increased temperatures, which can approach the melting temperature during friction stir welding, will not only further coarsen and transform the  $\theta'$  precipitates, but will also start to dissolve the precipitates. Upon cooling, fine GP zone precipitates form from the supersaturated solid solution thus formed. The greater number density of GP zone precipitates formed as a function of increasing peak temperature towards the weld center results in an increase in microhardness.

The typical fracture location of these friction stir welds (at the soft band located at the TMAZ/HAZ boundary) appears to be directly related to these microstructural evolutions. The lack of fine strengthening precipitates at the TMAZ/HAZ boundary, due to the coarsening of the

initial  $\gamma'$  precipitates and insufficient precipitate dissolution to form GP zones during cooling, reduces the strength of this location and makes it more susceptible to failure.

The microstructural evolutions also help elucidate the FSW process. The distribution of GP zones indicates that significant precipitate dissolution occurs in the TMAZ during welding. No evidence of precipitate dissolution is present in the HAZ, indicating that the precipitate dissolution is limited to the stir zone of the weld. While it is possible that the temperatures required for precipitate dissolution are coincidentally similar to those required for grain deformation, it is more likely that precipitate dissolution allows the larger-scale grain deformations to occur by reducing the strength of those regions. The deformation field would therefore be constrained at the HAZ, where precipitate dissolution was not as pronounced during welding.

A similar soft band was also located at the HAZ/TMAZ interface in a weld prepared at more than twice the weld speed (3.4 mm/s, 8 in/min, shown in Figure 15). The microstructurally equivalent regions of this weld were exposed to a shorter thermal cycle because of the increased weld speed. To compensate for this shorter thermal cycle, those microstructurally equivalent regions must also have been subjected to a higher peak temperature. Despite this, the soft band in this weld is again located at the TMAZ/HAZ boundary. Since the soft band was shown to correspond to the outer limit of precipitate dissolution, this supports the idea that the deformation field was limited to regions of the weld which had experienced significant precipitate dissolution during welding (i.e., the weld nugget and the TMAZ), and, conversely, that the deformation field was constrained by those regions (i.e., the HAZ) which did not experience significant precipitate dissolution.



#### IV. Conclusions

Microhardness mapping, crystallographic texture measurements, and microstructural analyses were used to systematically characterize the variations across the soft band in a friction stir weld in 2519 Al. The microhardness map revealed that the soft band, corresponding to the typical fracture location in friction stir welds of this alloy, is located at the boundary between the TMAZ and HAZ.

Texture analysis showed that the macroscopic rigid-body rotation of the base plate as material is drawn upward toward the stir zone accounts for much of the texture evolution in the TMAZ region. Delineation of the substructure by EBSD IQ mapping reveals evidence of increasing deformation in the TMAZ as the weld nugget is approached, and this is correlated with the remaining progressive texture evolution resulting from plastic spin. The stored deformation, however, is probably insufficient to significantly affect mechanical properties. Calculation of Taylor factors shows that texture variation does not substantially contribute to either the microhardness distribution or the transverse tensile failure behavior.

The primary cause of softening at the TMAZ/HAZ boundary was determined to be due to coarsening and transformation of the strengthening precipitates during the welding process. The initial distribution of fine  $\theta'$  precipitates in the base plate coarsens in the HAZ and experiences some transformation to the equilibrium  $\theta$  phase. Additional coarsening and transformation of the  $\theta'$  precipitates continue towards the weld center until no  $\theta'$  precipitates remain midway through the TMAZ. Locations within the TMAZ achieve temperatures during welding that are sufficient to at least partially dissolve the precipitates, leading to the precipitation of very fine GP zones during cooling. It is these GP zones that produce the observed hardening and strengthening in

the TMAZ. The observed minimum in microhardness therefore corresponds to the location that experienced the greatest coarsening and transformation of  $\gamma'$  precipitates yet which did not achieve sufficient temperatures to dissolve the precipitates and subsequently form GP zones during cooling.

These microstructural variations appear to cause the fracture of friction stir welds in this alloy to be localized at the TMAZ/HAZ boundary. This location experiences the greatest coarsening of the  $\gamma'$  precipitates before the fine GP zone precipitates begin to form. This fracture location therefore corresponds to the region with the least precipitate strengthening.

The development of the deformation field (stir zone) is also influenced by these microstructural evolutions. The presence of GP zones from the outer regions of the TMAZ toward the weld center demonstrate that significant precipitate dissolution occurred in those regions during welding. This indicates that dissolution of precipitates during welding allows the “stirring” deformation to occur and that undissolved precipitate distributions in the HAZ are sufficient to prevent that deformation.

## **Acknowledgements**

The authors would like to thank Harvey Castner, Tim Trapp, and Tim Stotler of the Navy Joining Center for providing the welds used in this study as well as for many productive discussions. We would also like to thank Sam Lambrakos and George Spanos for their helpful discussions and comments. Finally, we wish to thank Steve Linder of the ONR Programs Office for his support of this program. One of the authors (JFB) is supported through the U.S. Department of Energy, Los Alamos National Laboratory under Contract W-7405-Eng-36.



## References

1. W.M. Thomas, E.D. Nicholas, J.C. Needham, M.G. Murch, P. Templesmith, and C.J. Dawes, “Friction Stir Butt Welding”, International Patent Application No. PCT/GB92/02203 and GB Patent Application No. 9125978.8, Dec. 1991. U.S. Patent No. 5,460,317, Oct. 1995.
2. M.W. Mahoney, C.G. Rhodes, J.G. Flintoff, R.A. Spurling, and W.H. Bingel: *Metall. Mater. Trans. A*, 1998, vol. 29A, pp. 1955-1964.
3. B. Heinz, B. Skrotzki, and G. Eggler: *Mat. Sci. Forum*, 2000, vol. 331-337, pp. 1757-1762.
4. L.-E. Svensson, L. Karlsson, H. Larsson, B. Karlsson, M. Fazzini, and J. Karlsson: *Sci Tech. Weld. Join*, 2000, vol. 5, pp. 285-296.
5. A.P. Reynolds, W.D. Lockwood, and T.U. Seidel: *Mat. Sci. Forum*, 2000, vol. 331-337, pp. 1719-1724.
6. J.B. Lumsden, M.W. Mahoney, G. Pollock, and C.G. Rhodes: *Corrosion*, 1999, vol. 55, pp. 1127-1135.
7. L.E. Murr, G. Liu, and J.C. McClure: *J. Mat. Sci.*, 1998, vol. 33, pp. 1243-1251.
8. C.G. Rhodes, M.W. Mahoney, W.H. Bingel, R.A. Spurling, and C.C. Bampton: *Scripta Mater.*, 1997, vol. 36, pp. 69-75.
9. K.V. Jata, K.K. Sankaran, and J.J. Ruschau: *Metall. Mater. Trans. A*, 2000, vol. 31A, pp. 2181-2192.
10. G. Liu, L.E. Murr, C.-S. Niou, J.C. McClure, and F.R. Vega: *Scripta Mater.*, 1997, vol. 37, pp. 355-361.
11. Y.S. Sato, H. Kokawa, M. Enomoto, and S. Jogan: *Metall. Mater. Trans. A*, 1999, vol. 30A, pp. 2429-2437.

12. J.-Q. Su, T.W. Nelson, R. Mishra, and M. Mahoney: *Acta Mater.*, 2003, vol. 51, pp. 713-729.
13. T. Trapp and T. Stotler, EWI Project No. 43114GDE Report, January 2, 2003. p. 21.
14. Kallend, J.S., Kocks, U.F., Rollett, A.D., and Wenk, H.-R.: *Mat. Sci. Eng.*, 1991, vol. A132, pp. 1-11.
15. TSL/EDAX Orientation Imaging Microscopy manual, Draper, UT 2001.
16. B. L. Adams, S. I. Wright, and K. Kunze: *Metall. Trans. A*, 1993, vol. 24, pp. 819-831.
17. Taylor, G.I., *J. Inst. Metals*: 1938, vol. 62, pp. 307-324.
18. U.F. Kocks, G.R. Canova, C.N. Tomé, A.D. Rollett, and S.I. Wright: Computer Code LA-CC-88-6, Los Alamos National Laboratory, Los Alamos, NM.
19. A. Guinier, *Nature*: 1938, vol. 142, p. 569.
20. G.D. Preston, *Nature*: 1938, vol. 142, p. 570.
21. G.E. Dieter: *Mechanical Metallurgy*, 3rd ed., McGraw-Hill, New York, NY, 1986, p.213.

## Figure Captions

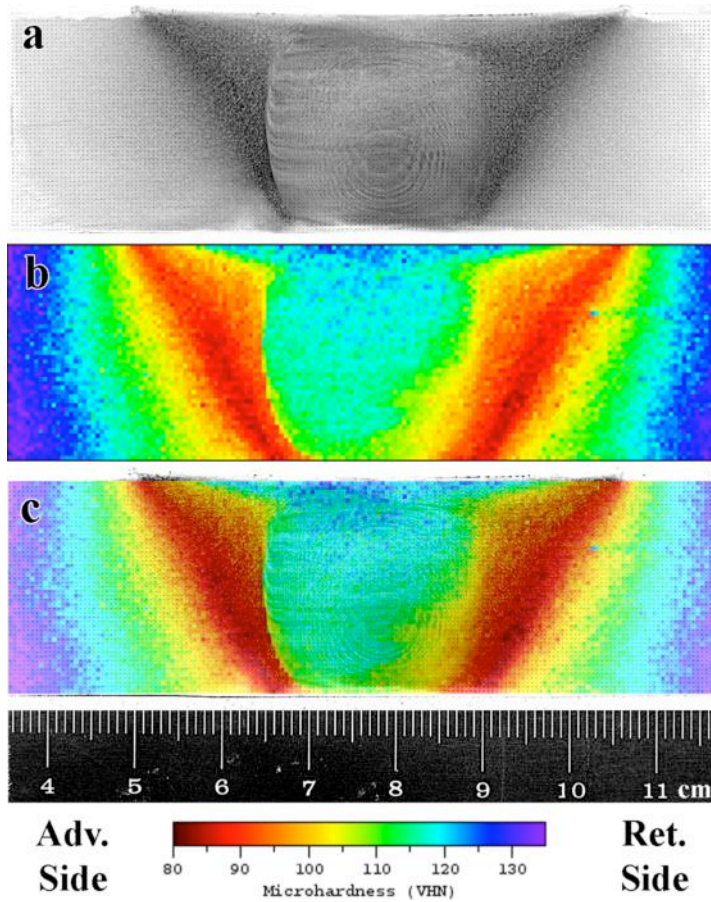


Figure 1. (a) Optical micrograph of the friction stir weld transverse cross section, (b) Microhardness map of the friction stir weld transverse cross section with a resolution of 0.5 mm in both directions, and (c) microhardness map superimposed on weld micrograph. Advancing side of the weld is on the left.

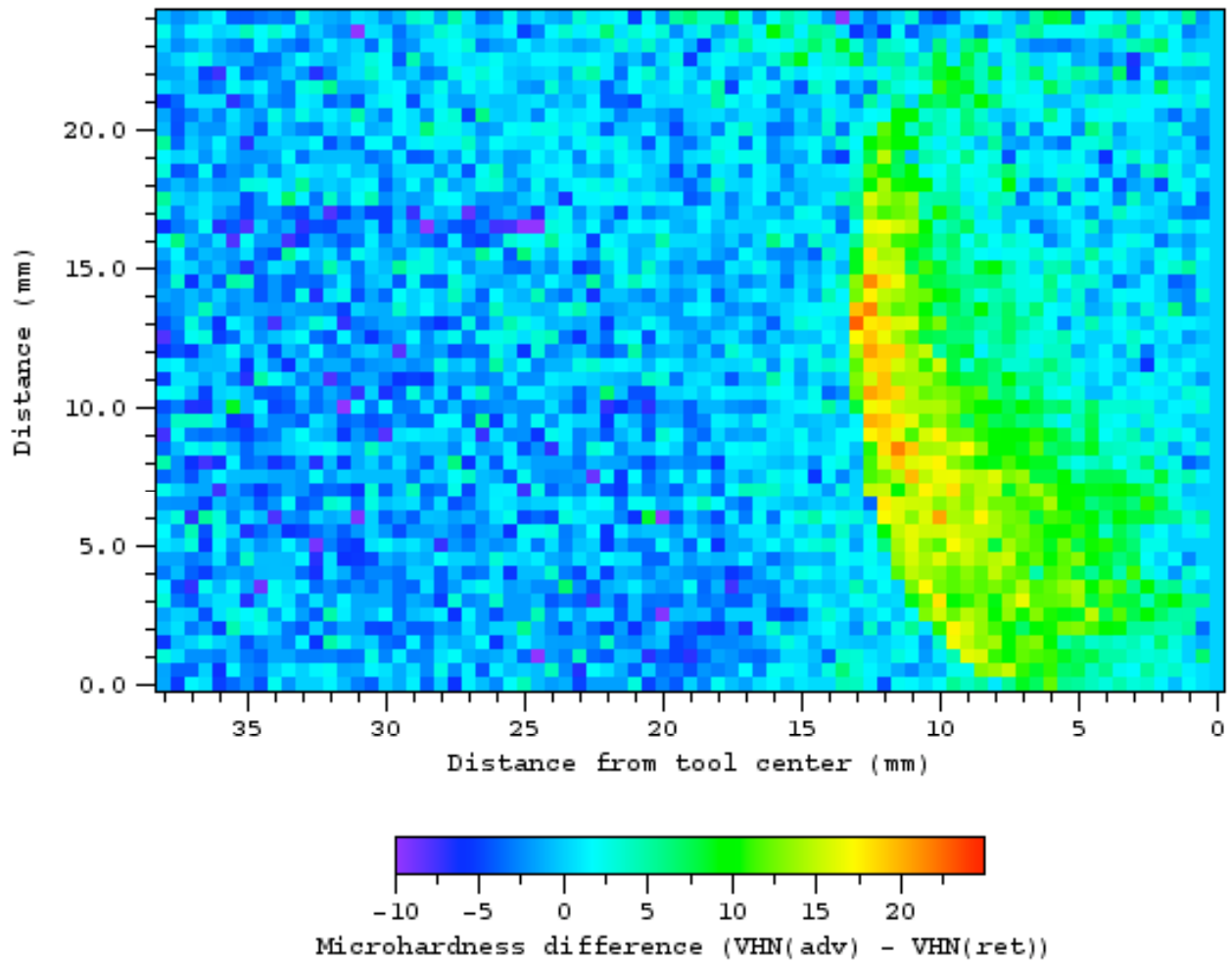


Figure 2. Map of the microhardness asymmetry across the friction stir weld, showing the difference between the advancing and retreating sides of the friction stir weld.

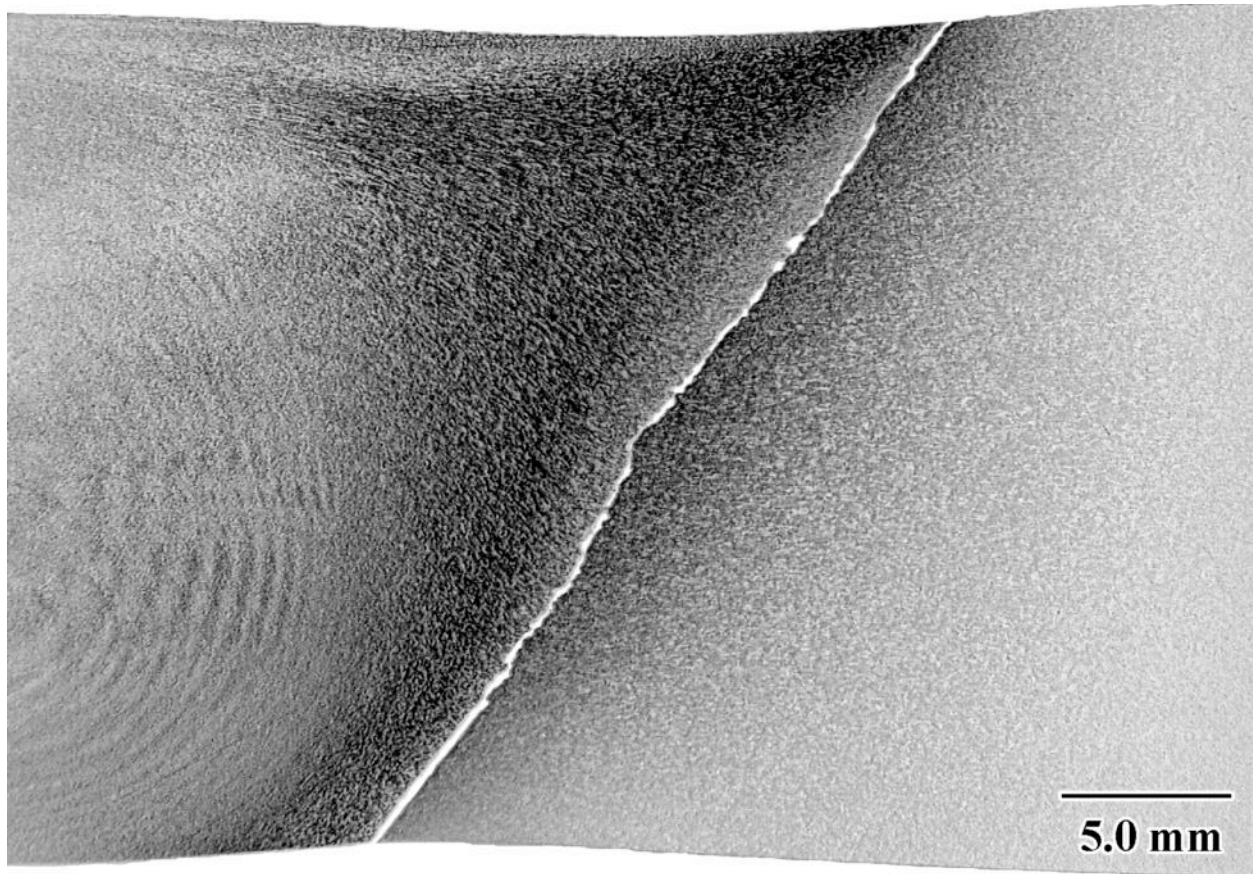


Figure 3. Optical micrograph of fracture location from the whole weld tensile test, showing fracture along the HAZ/TMAZ boundary on the retreating side.



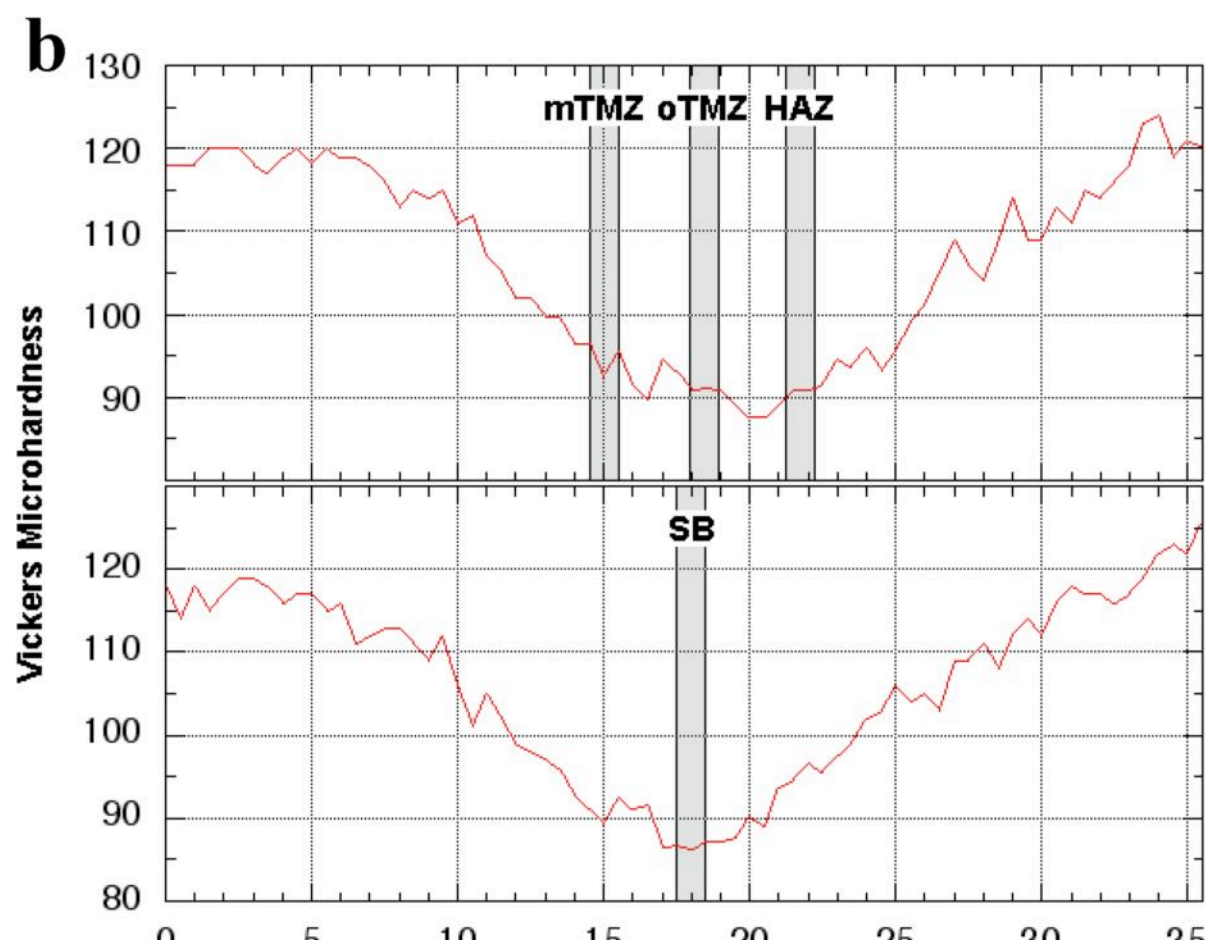
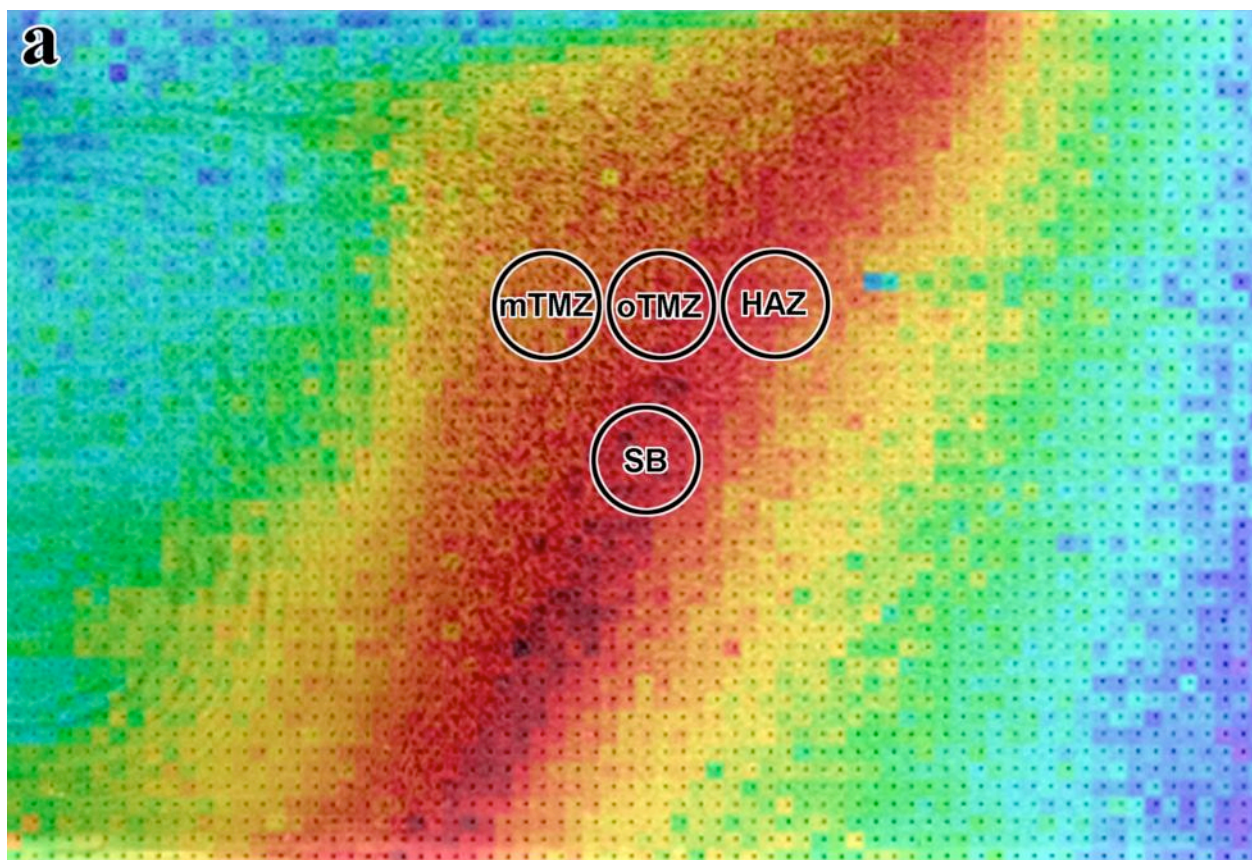


Figure 4. (a) Microhardness map superimposed on the weld micrograph of the retreating side of the friction stir weld, showing the locations of the regions examined in this study (microhardness scale shown in Figure 1), and (b) location of the center 1 mm of each region displayed on microhardness linescans through those regions.

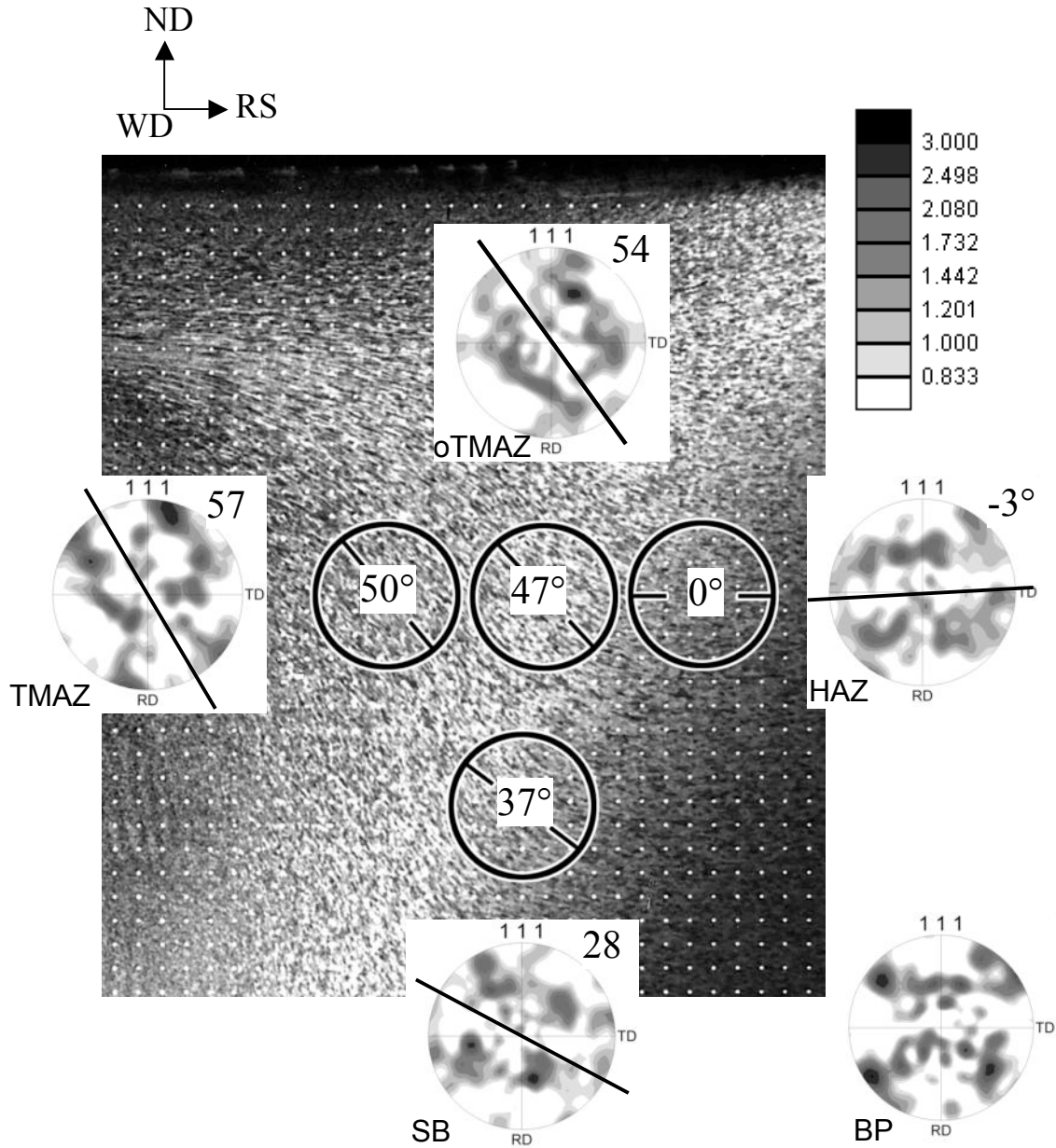


Figure 5. Optical micrograph of the retreating side of the FSW transverse cross section showing apparent inclination of grains based on visual inspection as a function of position in the weld (see text for identification). Associated 111 pole figures and apparent rotation of texture from BP are also shown for each region. Texture scale in multiples of random distribution.

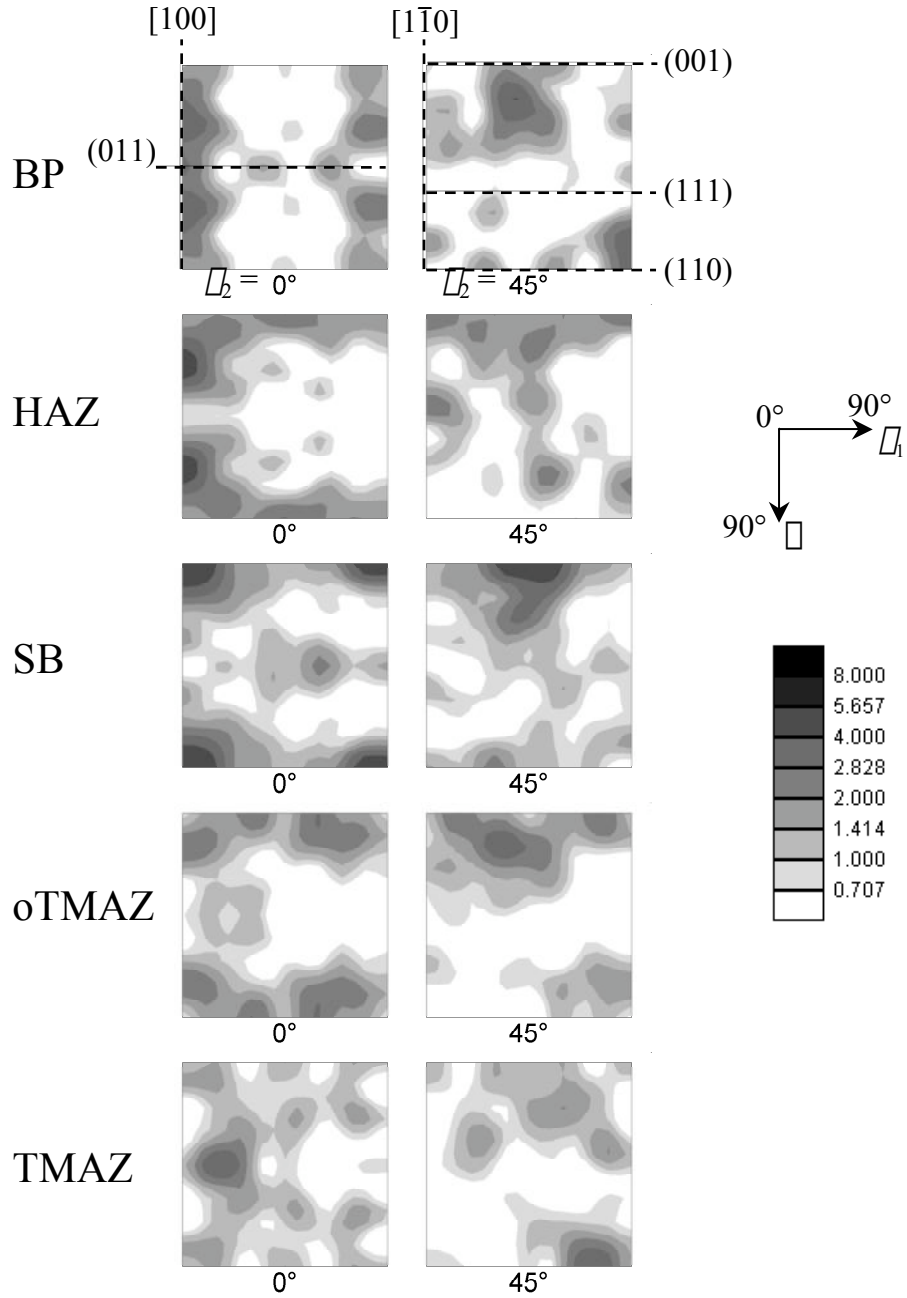


Figure 6. Constant  $\varphi_2$  sections (0° and 45°) of the orientation distribution of the retreating side of the FSW as a function of position in the weld (see text for identification). Prominent texture fibers are identified in the BP sections. Texture scale in multiples of random distribution.



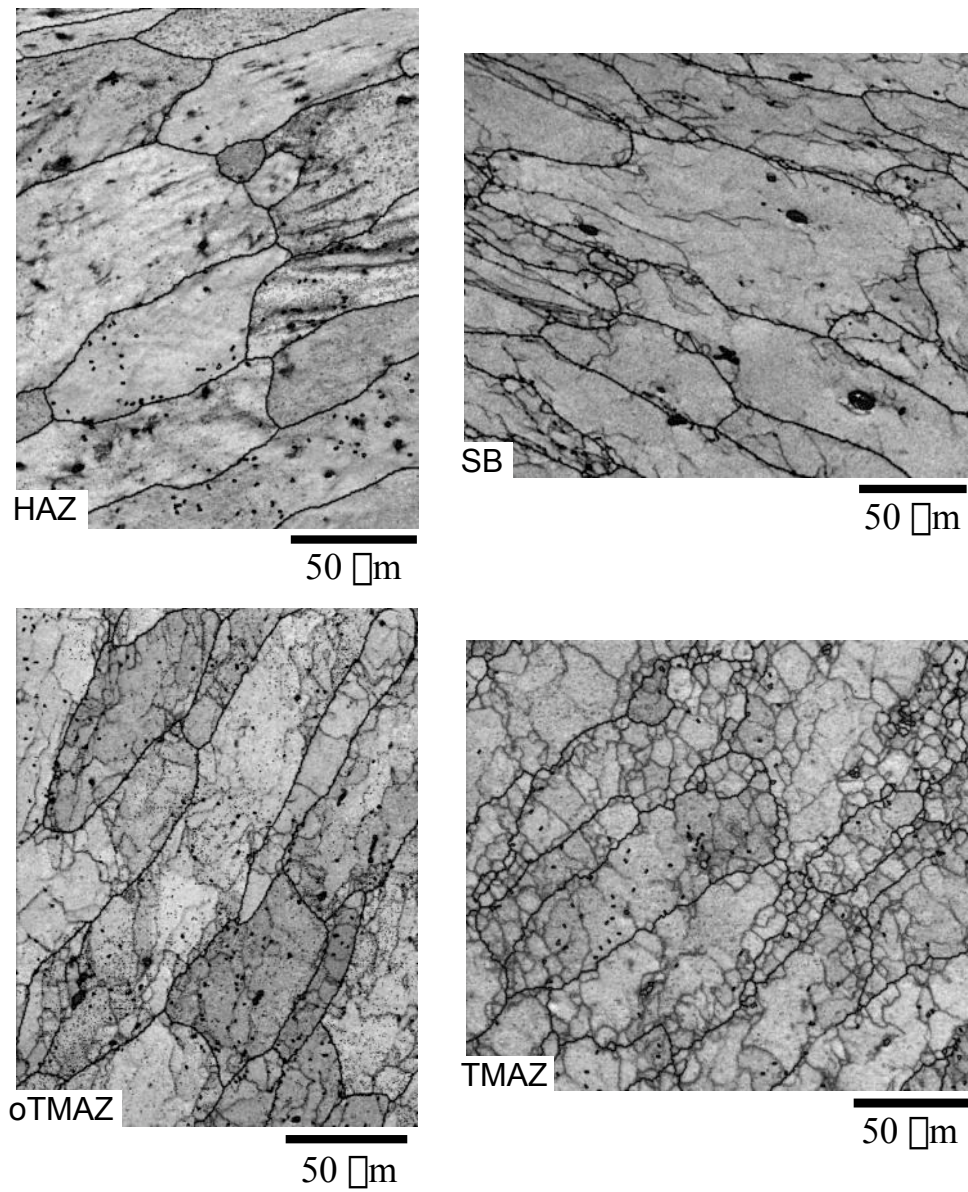


Figure 7. Image quality maps from regions in retreating side of FSW showing development of substructure as a function of position. Heavy boundaries are  $>15^\circ$  misorientation and light boundaries are  $2^\circ - 15^\circ$  misorientation.

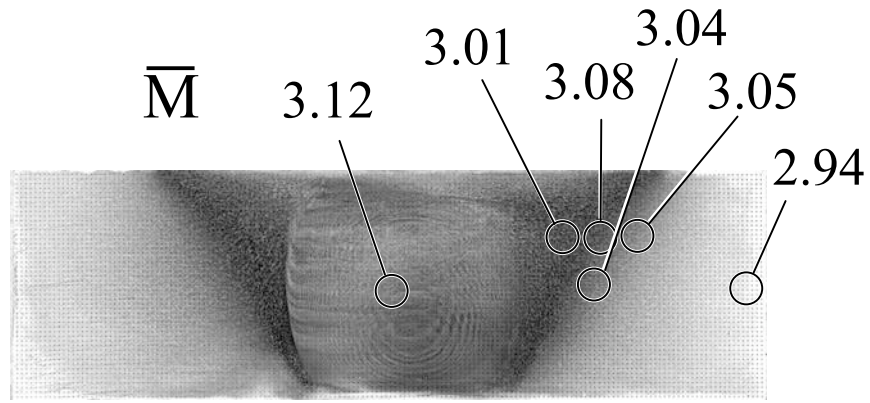


Figure 8. Cross-section macrograph of FSW showing average Taylor factor ( $\bar{M}$ ) for two principal directions of uniaxial strain as a function of position in the weld. ‘TD’ denotes strain in the transverse direction and ‘WD’ strain in the welding direction.

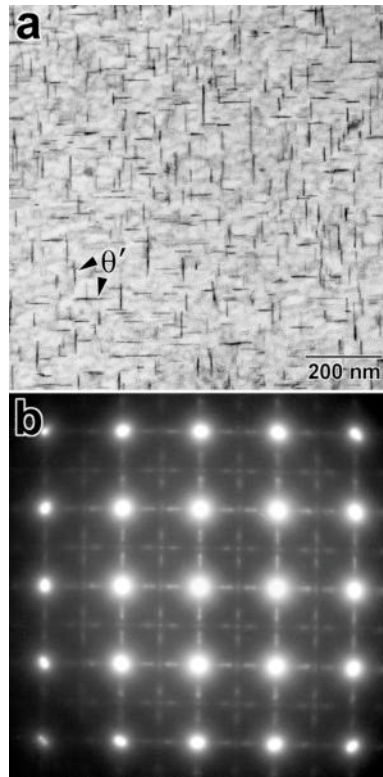


Figure 9. (a) TEM micrograph showing the fine  $\square$  precipitate distributions in the 2519-T87 base plate and (b) electron diffraction pattern from this region.

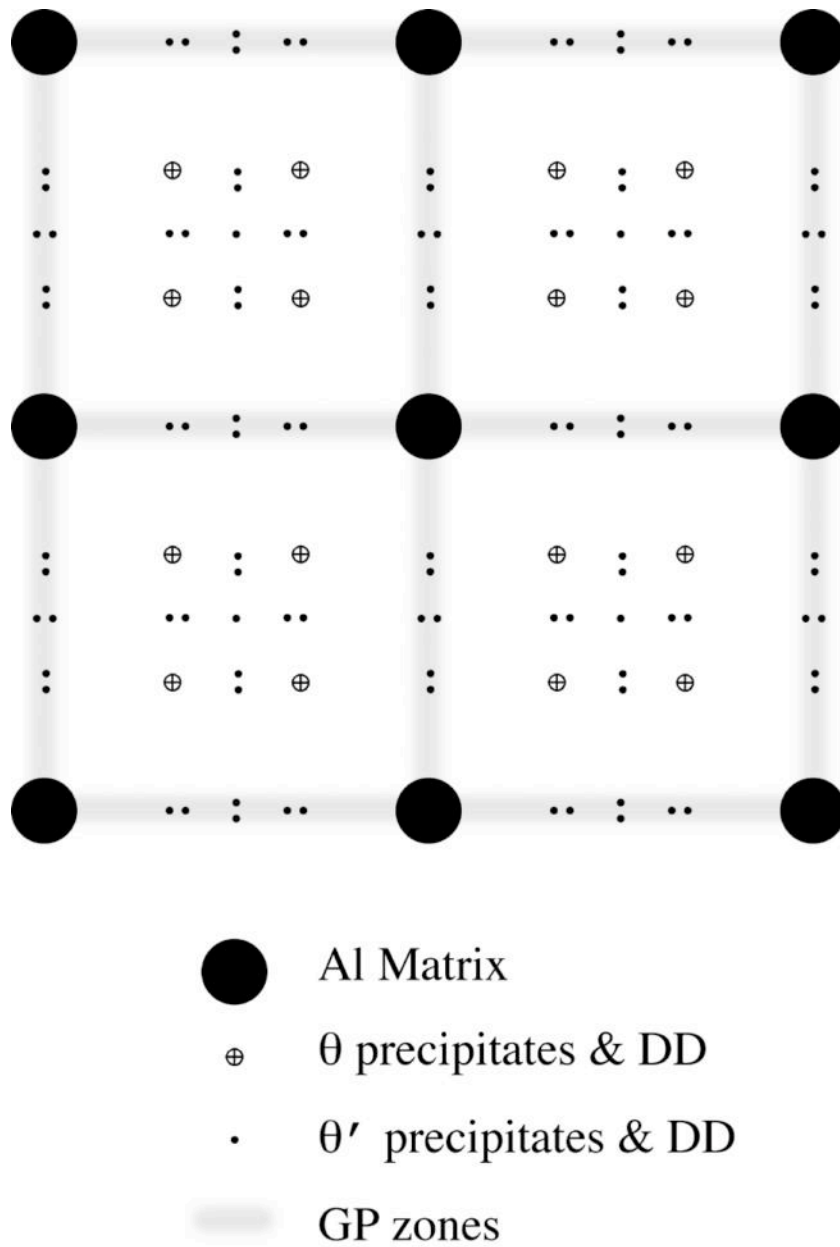


Figure 10. Schematic electron diffraction pattern showing  $\theta$ ,  $\theta'$ , and GP zone precipitate reflections and typical double diffraction relative to the aluminum matrix.

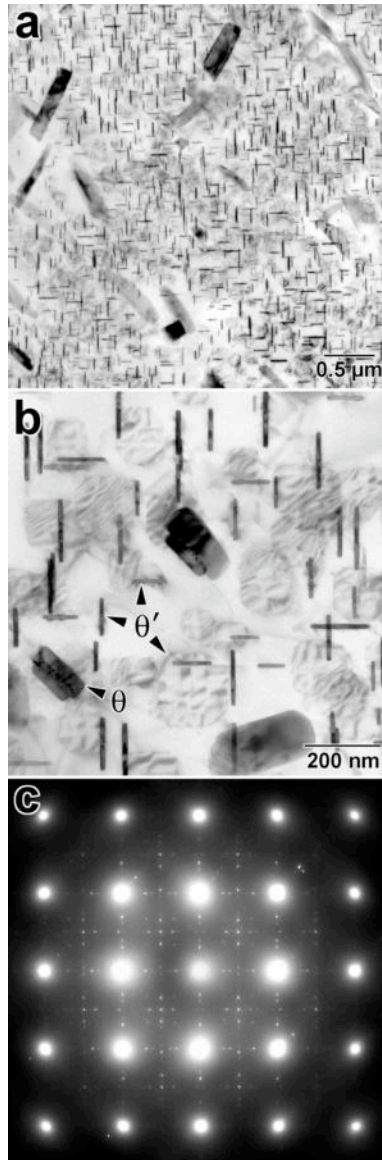


Figure 11. (a),(b) TEM micrographs showing the predominantly  $\square$  precipitate distributions in the HAZ and (c) electron diffraction pattern from this region.

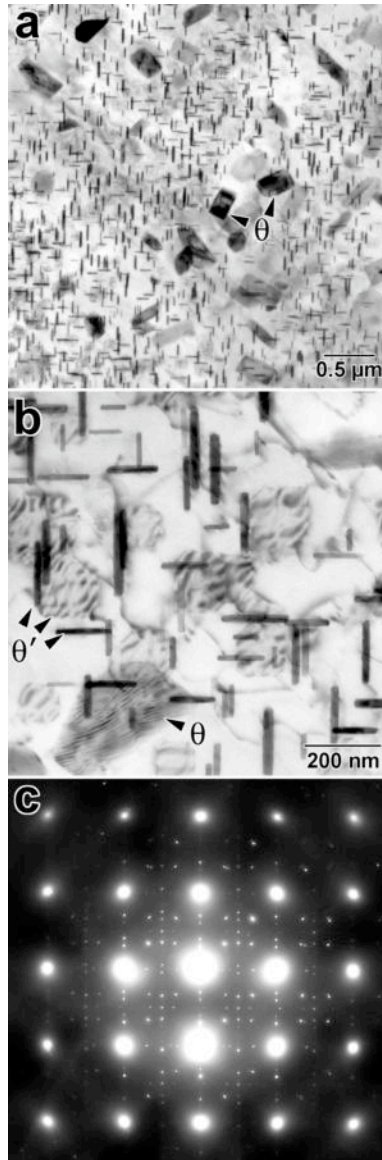


Figure 12. (a),(b) TEM micrographs showing the mixed  $\square$  and  $\square$  precipitate distributions in the soft band and (c) electron diffraction pattern from this region.



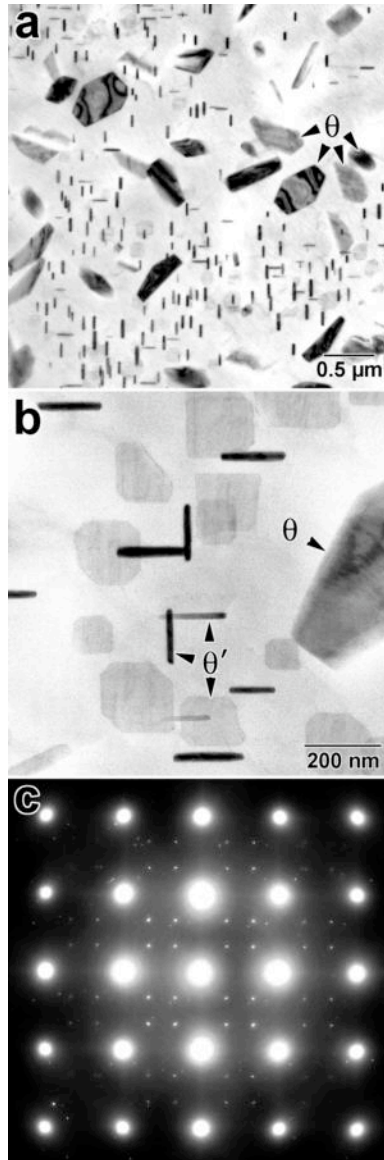


Figure 13. (a),(b) TEM micrographs showing the mixed  $\square$  and  $\square$  precipitate distributions in the outer TMZ and (c) electron diffraction pattern from this region ( $\square$  reflections not visible).

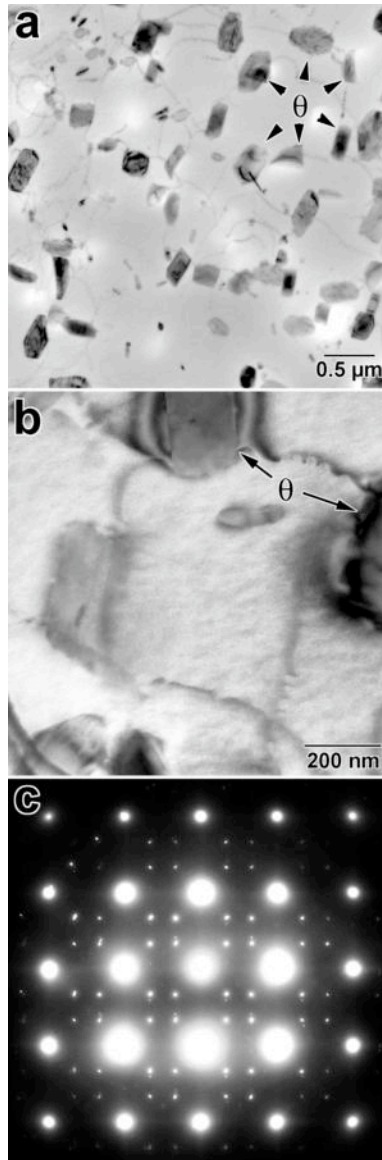


Figure 14. (a),(b) TEM micrographs showing the equilibrium  $\theta$  precipitate distributions in the middle TMZ and (c) electron diffraction pattern from this region.

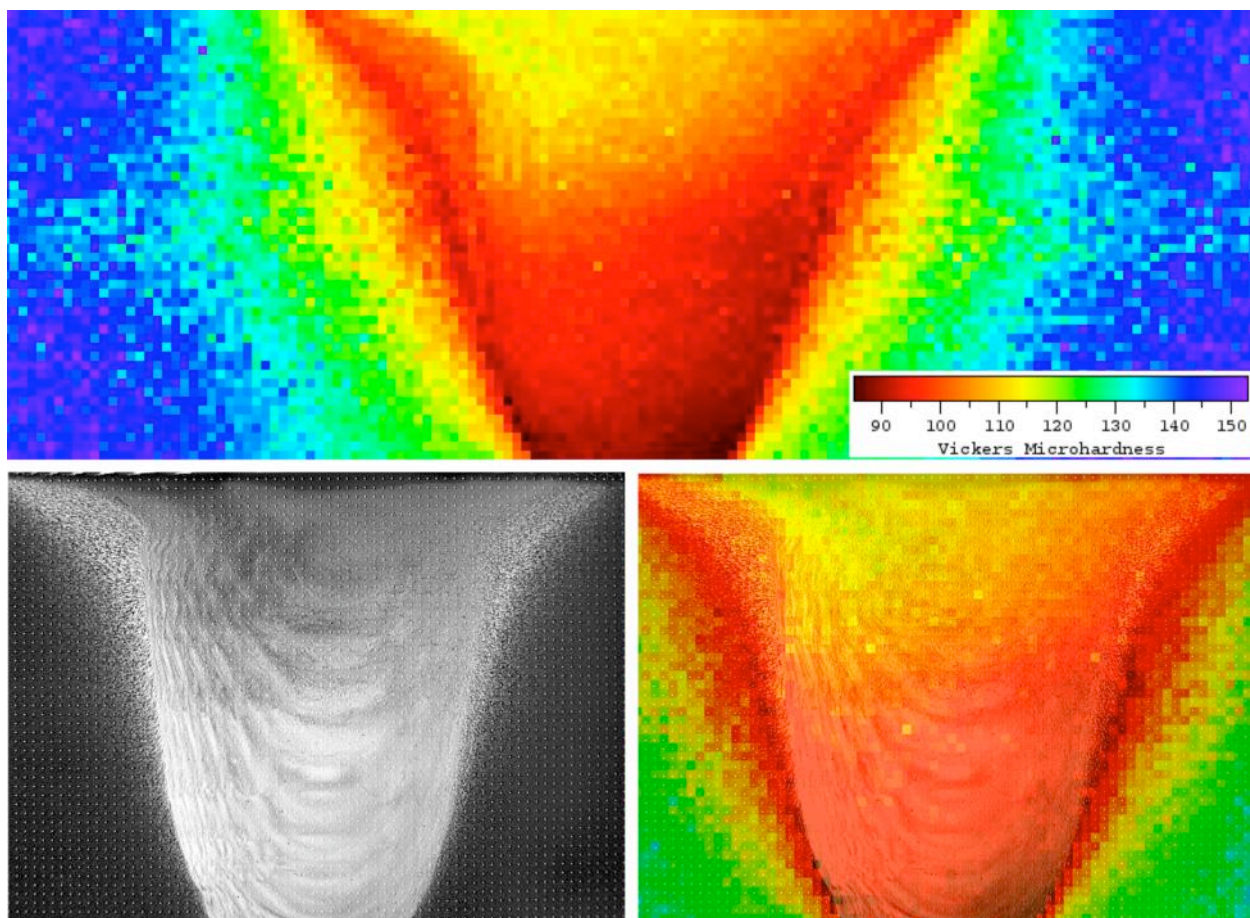


Figure 15. Optical micrograph, microhardness map, and superimposition of the microhardness map on the weld micrograph of a weld prepared at 3.4 mm/s (8 in/min).